Nanoscale Control of Optical Heating in Complex Plasmonic Systems

Guillaume Baffou,[‡] Romain Quidant,[‡,§] and F. Javier García de Abajo[†,*]

[†]Instituto de Óptica, CSIC, Serrano 121, 28006 Madrid, Spain, [‡]ICFO, Institut de Ciencies Fotòniques, 08860 Castelldefels, Barcelona, Spain, and [§]ICREA, Institució Catalana de Recerca i Estudis Avancats, 08010 Barcelona, Spain

ABSTRACT We introduce a numerical technique to investigate the temperature distribution in arbitrarily complex plasmonic systems subject to external illumination. We perform both electromagnetic and thermodynamic calculations based upon a time-efficient boundary element method. Two kinds of plasmonic systems are investigated in order to illustrate the potential of such a technique. First, we focus on individual particles with various morphologies. In analogy with electrostatics, we introduce the concept of thermal capacitance. This geometry-dependent quantity allows us to assess the temperature increase inside a plasmonic particle from the sole knowledge of its absorption cross section. We present universal thermal-capacitance curves for ellipsoids, rods, disks, and rings. Additionally, we investigate assemblies of nanoparticles in close proximity and show that, despite its diffusive nature, the temperature distribution can be made highly non-uniform even at the nanoscale using plasmonic systems. A significant degree of nanoscale control over the individual temperatures of neighboring particles is demonstrated, depending on the external light wavelength and direction of incidence. We illustrate this concept with simulations of gold sphere dimers and chains in water. Our work opens new possibilities for selectively controlling processes such as local melting for dynamic patterning of textured materials, chemical and metabolic thermal activation, and heat delivery for producing mechanical motion with spatial precision in the nanoscale.

KEYWORDS: plasmonics · optical heating · thermodynamics · nanophotonics boundary element method · nanoscale control

The control of optical-energy deposition by light absorption in nanostructures is emerging as a powerful tool in the manipulation of nanoscale thermally activated processes, with applications to areas such nanofluidics,[1,2] nanocatalysis,[3] photothermal cancer therapy,[4−6] drug delivery,[7,8] imaging and spectroscopy,[9−12] information storage[13] and processing,[14,15] and nanoscale patterning[16] (for example, *via* phase transitions).[17,18] In this context, plasmon-assisted photothermal processes configure the emerging field of thermoplasmonics,[19] in which light absorption and heat dissipation are competing mechanisms that rule the actual temperature distribution in metallic nanostructures. The goal is to use metal nanoparticles under external illumination as controlled nanosources of heat. To this end, plasmon resonances in noble metal nanoparticles are ideally located in the visible and near-infrared regions of the spectrum, and they can be tuned by changes in size, morphology, and composition, over which a large degree of control has been achieved in recent years through colloidal chemistry[20] and nanolithography.[21]

Despite the intensity of these efforts, a quantitative analysis of the actual temperature increase and its spatial distribution remains challenging, with most works only reporting qualitative changes or empirical data, except for spherical particles.[17] In the case of continuous-wave external illumination, one just needs to solve the steady-state heat transport equation with the source supplied by light absorption. This has analytical solution for spheres, but it requires using numerical tools for other geometries.

Here, we provide a numerical tool to quantitatively explore the temperature distribution in arbitrarily complex assemblies of plasmonic nanoparticles exposed to external illumination. The technique is time-efficient and applies to any geometry. Under stationary conditions, the partial absorption cross sections of nanoparticles are calculated using a boundary element method (BEM).[22,23] From this, because the heat transport equation is formally equivalent to Poisson's equation (*i.e.*, to the electrostatic limit of the electromagnetic problem), we calculate the temperature profile using the same BEM in the low-frequency limit, $\omega \to 0$. Two different situations are addressed within this paper: isolated nanoparticles with nontrivial morphology and sphere assemblies in close proximity.

*Address correspondence to jga@cfmac.csic.es.

Received for review September 2, 2009 and accepted December 30, 2009.

Published online January 7, 2010. 10.1021/nn901144d

RESULTS AND DISCUSSION

Steady-State Model. In the steady-state regime, the thermal diffusion equation reduces to[17,24]

$$\nabla\cdot[\kappa(\mathbf{r})\nabla T(\mathbf{r})] = -p(\mathbf{r}) \quad (1)$$

where $T(\mathbf{r})$ is the distribution of temperature produced by an external heat source of power density $p(\mathbf{r})$ in an inhomogeneous medium characterized by a position-dependent thermal conductivity $\kappa(\mathbf{r})$. This is formally equivalent to Poisson's equation, with κ playing the role of the local permittivity, T the potential, and $p/4\pi$ the external charge. In our case, the source of heat is due to optical absorption, which is locally proportional to the electric field intensity and the imaginary part of the dielectric function ε.[19] For monochromatic light of frequency ω and time-dependent electric field $\mathbf{E}(\mathbf{r},t) = 2\mathrm{Re}\{\mathbf{E}(\mathbf{r})\exp(-i\omega t)\}$, one has (in Gaussian units)

$$p(\mathbf{r}) = \frac{\omega}{2\pi}\mathrm{Im}\{\varepsilon(\mathbf{r},\omega)\}|\mathbf{E}(\mathbf{r})|^2$$

In the following, we consider gold nanoparticles immersed in water. We can safely ignore absorption in water and therefore consider the source of eq 1 to be fully contained inside the particles. Interestingly, the absorption power density $p(\mathbf{r})$ is markedly non-uniform,[19] especially near gaps and corners, but the resulting temperature distribution is smooth due to the large contrast of thermal conductivities between gold and water ($\kappa_{gold} = 318\ \mathrm{Wm^{-1}\,K^{-1}} \gg \kappa_{water} = 0.6\ \mathrm{Wm^{-1}\,K^{-1}}$): in the language of thermal diffusion, heat flows so fast inside the particle, compared to the outside medium, that its temperature is nearly uniform for moderate particle size, and thermal energy accumulates at the particle boundary before it diffuses away through the water; and in the language of electrostatics, interpreting eq 1 as Poisson's equation, the particle behaves as a perfect electric conductor that maintains a uniform *potential* (*i.e.*, temperature). This uniform-temperature approximation (UTA) is rather accurate for good thermal conductors, as we show below.

We solve Maxwell's equations to obtain p, which we input in turn into eq 1 to determine T using the same BEM[22,23] in the $\omega \to 0$ limit. In the BEM, the fields are expressed in terms of boundary sources, which are determined self-consistently by imposing the customary boundary conditions. Further details of the BEM can be found in ref 23.

It should be noted that this formalism cannot be generalized to widely illuminated objects of infinite extension. For example, a uniformly illuminated infinite rod responds to Poisson's equation for a uniformly charged infinite wire, which produces a potential (*i.e.*, a temperature increase) that grows as log (r) with the distance to the wire, and therefore, the steady-state solution of this problem involves an infinite temperature increase in the wire with respect to distant points of the surrounding medium. Similarly, an infinite planar surface under uniform illumination cannot reach a steady-state distribution of temperatures, but rather, it heats up continuously.

Time Needed To Reach a Steady-State Temperature Distribution. It is useful to estimate the time required to reach the steady-state temperature distribution that we consider in this work. During the transient state, the temperature distribution throughout the particle and its surroundings is governed by the time-dependent heat equation

$$\rho c_p \partial T/\partial t + \nabla\cdot[\kappa\nabla T] = -p$$

where ρ is the mass density (kg m^{-3}) and c_p the thermal capacity (J kg^{-1} K^{-1}). Dimensional analysis of this equation leads to an estimate of the typical time scale τ required to reach the steady-state regime:

$$\tau \sim R^2\frac{\rho c_p}{\kappa} = \frac{R^2}{D}$$

where D is the so-called thermal diffusivity (m^2 s^{-1}) and R is a typical length of the system, such as the radius of the particle in the case of a sphere. Since thermal processes are much faster in the metal, the surrounding water medium governs the magnitude of the transient time scale, and we can write $\tau \sim R^2/D_{water}$. Using $D_{water} = 1.43 \times 10^{-8}\ \mathrm{m^2\,s^{-1}}$ and $R = 50$ nm, we find $\tau \sim 0.1\ \mu$s. This time scale is compatible with temporal modulation of the external light, which might be a source of interesting effects, but it is negligible under typical continuous-wave illumination conditions. It should be noted that the quadratic dependence R^2 makes this time scale highly dependent on the size of the system. This estimate of τ is reasonable to describe the particle and its neighborhood, but it should be noted that the amount of thermal energy stored in the host medium becomes infinite under stationary conditions (see below).

Optical Heating of a Gold Sphere in Water. We start our discussion with the simple case of a spherical gold particle of radius R. Under the UTA, eq 1 produces a profile of temperature increase ΔT given by a Coulomb potential outside the particle

$$\begin{aligned}\Delta T(r) &= \Delta T_{NP}\frac{R}{r}, & r > R\\ &\approx \Delta T_{NP}, & r < R\end{aligned} \quad (2)$$

where ΔT_{NP} is the uniform temperature increase of the nanoparticle, generated by the total absorption power P (*i.e.*, the equivalent of the total electric charge in the electrostatics analogy). More precisely

$$P = \int \mathrm{d}\mathbf{r}\, p(\mathbf{r}) = \sigma_{abs} I$$

where σ_{abs} is the absorption cross section (we obtain this quantity numerically using BEM) and I is the irradiance of the incoming light (this is fixed by the experimental setup). Relating this to the Coulomb potential

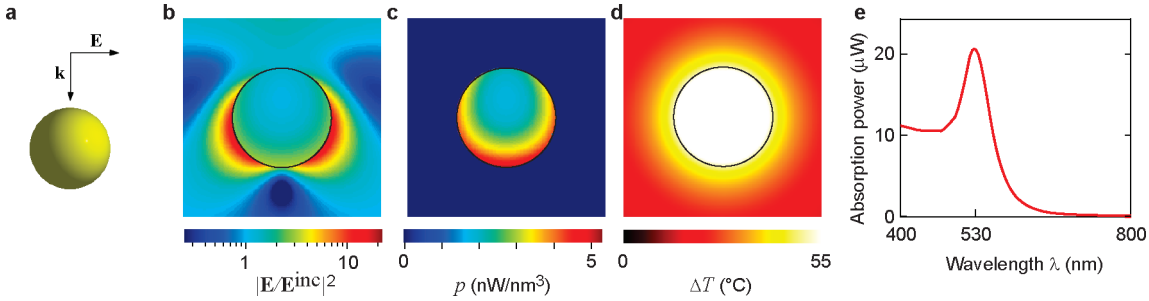

Figure 1. Photothermal heating of a 100 nm gold nanosphere placed in water. (a) Schematic representation of the sphere showing the orientation of the external electric field E and the light wavevector k. (b) Electric near-field intensity normalized to the incident field intensity, (c) heat generation density, and (d) equilibrium distribution of temperature increase for a light wavelength λ = 530 nm, tuned to the particle dipole plasmon. (e) Absorption power as a function of light wavelength. The incident light intensity is 1 mW /μm² in all cases.

produced by a uniformly charged sphere in a homogeneous medium of effective permittivity κ_{water}, we find[25]

$$\Delta T_{NP} = \frac{\sigma_{abs} I}{4\pi R \kappa_{water}} = \frac{P}{4\pi R \kappa_{water}} \quad (3)$$

Incidentally, the $1/r$ dependence of $\Delta T(r)$ outside the particle leads to an infinite amount of thermal energy stored in the surrounding medium.

Figure 1 illustrates the different field profiles involved for a 100 nm gold sphere. The absorption power density is $p \sim 1$ nW/nm^3, the absorption power is $P \sim 1$ μW, and the temperature increase is $\Delta T \sim 50$ K for an illumination intensity of 1 mW/ μm^2. Panels b−d of Figure 1 are obtained for the wavelength of maximum absorption, λ = 530 nm (Figure 1e). In the long-wavelength limit, one would find a uniform electric field inside the particle, but retardation effects lead to significant non-uniformity in the absorption density (Figure 1c). However, under the UTA, the temperature profile is uniform inside the particle and described by eq 2 outside it (Figure 1d).

Validity of the Uniform-Temperature Approximation (UTA). Since the temperature distribution responds to Poisson's equation, which is scale invariant, it depends on particle size only indirectly through the size dependence of the absorption power density. For a small sphere, $p(\mathbf{r})$ is uniform and the temperature increase inside it ($r < R$) becomes

$$\Delta T(r) = p(R^2 - r^2)/6\kappa_{gold} + \Delta T_{NP}$$

where ΔT_{NP} is given by eq 3. The temperature is maximum at the center of the particle, and it converges to ΔT_{NP} at the particle surface, but the thermal inhomogeneity is small, as illustrated by the ratio $\Delta T_{max}/\Delta T_{min} - 1 = \kappa_{water}/2\kappa_{gold} \approx 10^{-3}$. Even for relatively large spheres like that of Figure 1, the inhomogeneity of $p(\mathbf{r})$ (Figure 1c) translates just into a minor increase in $\Delta T_{max}/\Delta T_{min} - 1 = 0.0013$.

We put the UTA to a test for a more challenging situation in Figure 2, in which we consider an extreme distribution $p(\mathbf{r})$ consisting of a point source located at the center of one of the hemispheres defining the ends of a gold rod with hemispherical caps. The figure represents the thermal inhomogeneity defined by $|\Delta T_1 - \Delta T_2|/(\Delta T_1 + \Delta T_2)$, where ΔT_j are the temperature increments at the apex of the rod ends, as a function of the rod aspect ratio. The inhomogeneity remains low (<0.1) up to an aspect ratio of ≈10, and it gradually increases as the rod becomes more elongated, slowly evolving toward the asymptotic value of 1, which corresponds to no heating of the rod end opposite to the source. Despite the divergence of ΔT at the point source location, it should be noted that the definition of thermal inhomogeneity given above is not very sensitive to the actual location of the source as long as it is close to the particle end because the direct field of the source is efficiently quenched by the large value of κ_{gold}, and an induced thermal source is transferred to the surface to produce a dominant induced thermal field, in agreement with the nearly perfect-thermal-conductor behavior of the metal relative to the surrounding water.

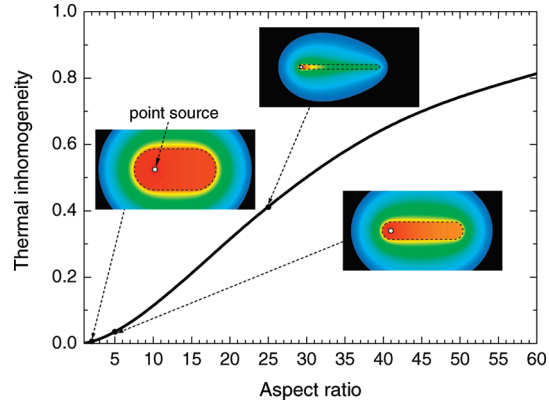

Figure 2. Temperature distribution in gold rods and limits of validity of the uniform-temperature approximation (UTA). We consider rods of hemispherical ends, exposed to a thermal point source located at the center of one of the hemispherical caps. The figure represents the thermal inhomogeneity, $|\Delta T_1 - \Delta T_2|/(\Delta T_1 + \Delta T_2)$, where ΔT_j are the temperature increments at the apex of the rod ends. The insets show the temperature distribution for various aspect ratios.

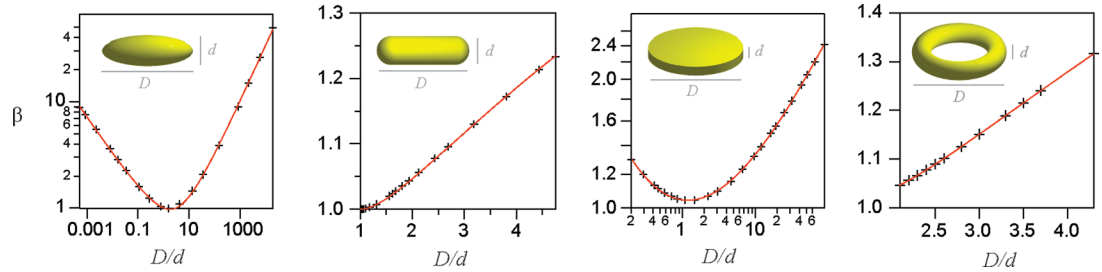

Figure 3. Universal dimensionless thermal-capacitance coefficient β for ellipsoids, rods with hemispherical caps, disks, and rings as a function of their aspect ratio *D*/*d* (see insets). This coefficient relates the temperature increase of an irradiated nanoparticle to the absorption power and the thermal conductivity of the surrounding medium, according to eq 4. We show numerical simulations (symbols) compared to the fitting functions of Table 1 (curves). The value of β is given for a particle of volume equal to that of a sphere of equivalent radius $R_{eq} = (d^2D/8)^{1/3}$ for ellipsoids, $R_{eq} = [(3D - d)d^2/16]^{1/3}$ for rods, $R_{eq} = (3D^2d/16)^{1/3}$ for disks, and $R_{eq} = (3\pi d^2D/16)^{1/3}$ for rings.

The situation considered in Figure 2 resembles the case of rods exposed to a light beam focused at one of the ends. The thermal inhomogeneity under more extended illumination should be, therefore, below the values reported in this figure. The particles that we consider below have aspect ratios fully compatible with the UTA.

Thermal Capacitance and Temperature Increase in Arbitrarily Shaped Particles. Continuing the analogy with electrostatics, we can define the thermal capacitance $C_{th} = P/\Delta T_{NP}$. The higher C_{th}, the lower the temperature increase for a given absorption power P. In particular, for a sphere, we obtain from eq 3

$$C_{th}^{sphere} = 4\pi R\kappa_{water}$$

where we observe a linear dependence on the thermal conductivity of the surrounding medium (water in our case). C_{th} depends only on the geometry of the particle and maintains this linear dependence on κ_{water}. For nonspherical shapes, we obtain C_{th} from BEM (in the $\omega \to 0$ limit) under the UTA, and we can write it in terms of a dimensionless thermal-capacitance coefficient β, implicitly defined by

$$C_{th} = 4\pi R_{eq}\beta\kappa_{water}$$

where R_{eq} is chosen as the radius of a sphere with the same volume as the particle. Then, the temperature increase at the metal can be written

$$\Delta T_{NP} = \frac{\sigma_{abs} I}{4\pi R_{eq}\beta\kappa_{water}} \qquad (4)$$

while the temperature far from the metal is still given by a Coulomb potential as

$$\Delta T(r) \approx \frac{\sigma_{abs} I}{4\pi r\kappa_{water}}, \qquad r \gg R_{eq} \qquad (5)$$

Notice that β does not appear in this latter formula. Figure 3 shows the calculated value of β for several common morphologies (ellipsoids, rods with hemispherical caps, disks, and rings) as a function of the aspect ratio *D*/*d*, where *D* and *d* are two geometrical parameters that unambiguously define each particle (see insets in Figure 3). Furthermore, we provide in Table 1 fitting functions corresponding to the four cases considered in Figure 3. The sphere is recovered from ellipsoids and rods for $D = d$, leading to $\beta = 1$. Interestingly, $\beta \geq 1$ in all cases because the sphere is the least efficient geometry in terms of heat dissipation: when deviating from the spherical shape, the thermal capacitance increases and the temperature is lower for fixed P, due to the increase in surface-to-volume ratio with respect to the sphere, which leads to more efficient heat release from the particle. Incidentally, in the UTA, the value of β does not depend on any structure that the particle might have in its interior, and in particular, spherical shells behave the same as spheres in this respect, with $\beta = 1$.

Optical Heating of Particle Assemblies. The accuracy of the UTA makes single nanoparticles unpractical for producing strong temperature gradients. However, we show next that assemblies of separated nanoparticles, even in close proximity, can be used for simultaneously controlling the temperature at different locations because the poor conductance of the surrounding medium prevents interparticle thermalization to a certain extent. Each particle j of an assembly of nanoparticles subject to external illumination absorbs a power $P_j =$

TABLE 1. Fitting Functions of the Dimensionless Thermal-Capacitance Coefficient β for the Structures Considered in *Figure 3*, As a Function of Their Aspect Ratio D/*d*

ellipsoid:	$\beta = \exp\{\sqrt{1+0.0416\ln^2(D/1.85d)} + 0.092\ln(D/1.85d) - 1\}$
rod:	$\beta = 1 + 0.96587\ln^2(D/d)$
disk:	$\beta = \exp\{0.040 - 0.0124\ln(D/d) + 0.0677\ln^2(D/d) - 0.00457\ln^3(D/d)\}$
ring:	$\beta = 1.021 + 0.17442\ln^2(D/d - 0.625)$

$\sigma_{abs,j}I$, which is proportional to the partial absorption cross section $\sigma_{abs,j}$ of that particle. We obtain the latter from the integral of the Poynting vector over the particle surface. This procedure gives an exact solution of the plasmonic problem, which we have checked by comparing BEM calculations to extended Mie theory calculations[26] (the results look identical on the scale of the figures). By analogy to electrostatics, the linear relation between absorption power and temperature increase can be written as

$$P_j = \sum_{j'} C_{th,jj'} \Delta T_{j'} \qquad (6)$$

where $\Delta T_{j'}$ is the temperature increase of particle j' and $C_{th,jj'}$ are coupled thermal capacitances. We find $C_{th,jj'}$ for each j by solving eq 1 while artificially setting $P_{j'} = 0$ for $j' \neq j$. Once these coefficients are determined, the temperature variation of each particle is obtained from the partial absorption powers by inversion of eq 6.

Gold Sphere Dimer. We start for simplicity by analyzing dimers consisting of two 100 nm gold spheres separated by a surface-to-surface gap distance d and illuminated as sketched in Figure 4a. Our goal is to demonstrate the possibility of independently controlling the temperature increase in both spheres by playing with the illumination wavelength and direction of incidence.

We first explore in Figure 4 the dependence of the thermal effects on gap distance. Figure 4b,c represents the temperature of each of the two spheres as a function of wavelength and d. The magnitude of the temperature increase shows a prominent feature at a wavelength of 540 nm, which red shifts as the particles separate. This is closely following the profile of the dominant dipole mode in a sphere dimer.[27] It is, however, more interesting to look at the ratio of partial absorption rates (Figure 4d) and the ratio of temperature variations (Figure 4e). The ratio of temperatures follows approximately, but not completely, the ratio of absorption powers. In particular, even though the absorption ratio can reach 1.47, the maximum temperature ratio is lowered down to 1.25 due to interparticle thermal interaction. This is just an example of how thermal coupling between particles is an unavoidable element in particle arrays. Interestingly, the temperature of a given particle can be made either smaller or larger than in the other particle by adjusting the wavelength for each separation distance.

For fixed gap distance, we can achieve a substantial degree of control over the temperature of each of the dimer particles by changing the wavelength and the angle of incidence of the external light, as shown in Figure 5. The absorption cross section and the extinction cross section of the entire dimer, represented in Figure 5a,b, exhibit a dominant feature near 580 nm that is most intense for incidence along the dimer axis. The extinction shows an additional feature centered at 615 nm, with a maximum for incidence normal to the dimer axis (external field aligned with the dimer), although it does not produce absorption and it is thus entirely due to scattering. The ratios of absorption powers and particle temperature variations represented in Figure 5c,d show that, for a wavelength of 550 nm and incidence along the dimer axis, the far sphere has a temperature 1.4 times lower than that of the near sphere. The near-field and the temperature distribution corresponding to this configuration are shown in Figure 5e,g, pointing out a clear shadowing effect of the upper sphere over the lower one. This situation is reversed for oblique incidence at 650 nm, with the lower sphere picking up a larger field intensity and therefore featuring higher temperature (Figure 5f,h). For incidence angles below $\theta = 45°$, the tempera-

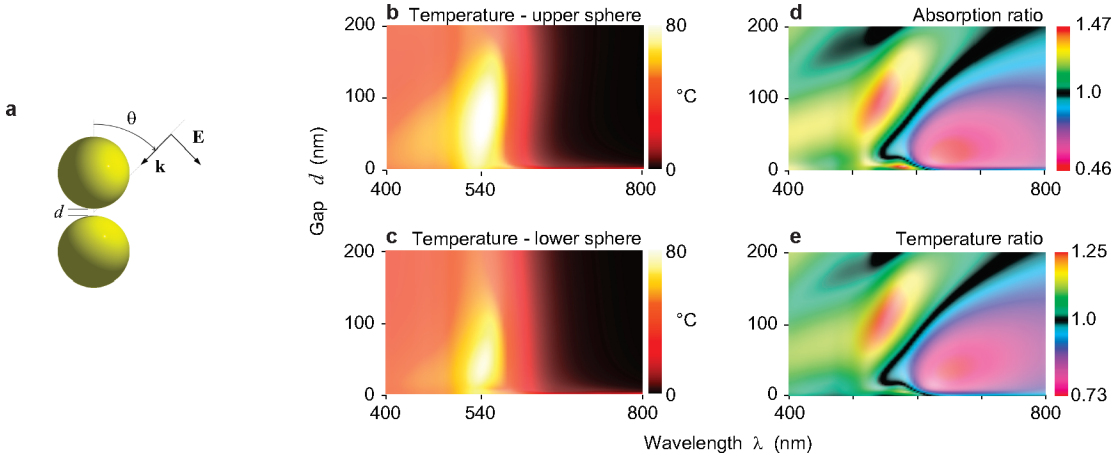

Figure 4. Increase in temperature at each of the 100 nm spheres forming a water-immersed gold dimer as a function of light wavelength λ and gap distance d between particle surfaces. (a) Sketch of the dimer, illuminated by a 1 mW/μm² p-polarized light plane-wave under an angle of incidence θ = 45° with respect to the axis or rotational symmetry. (b,c) Temperature increase in the upper and lower spheres, ΔT_{up} and ΔT_{down}, respectively. (d) Ratio of the partial absorption cross sections of the upper and lower spheres. (e) Ratio of temperature increase, $\Delta T_{up}/\Delta T_{down}$.

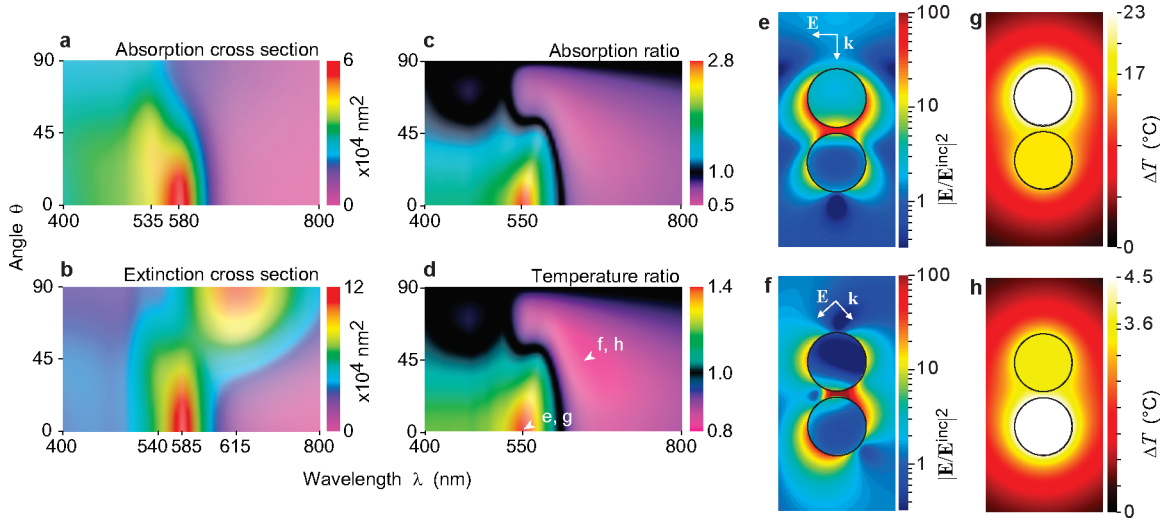

Figure 5. Increase in temperature at each of the 100 nm spheres forming a water-immersed gold dimer as a function of light wavelength λ and angle of incidence θ for fixed gap distance between sphere surfaces d = 10 nm (see Figure 4a). (a,b) Light absorption and extinction cross sections of the dimer, respectively. (c) Ratio of the partial absorption cross sections of the upper and lower spheres. (d) Ratio of temperature increase. (e) Electric near-field intensity for θ = 0 (see inset) and λ = 550 nm, normalized to the external field intensity. (f) Same as (e), for θ = 45° and λ = 650 nm. (g,h) Distribution of temperature increase under the illumination conditions of (e) and (f), respectively. (e−h) Correspond to the conditions signaled by short arrows in (d). The incident light intensity is 1 mW/μm² in all cases.

ture ratio can be tuned by playing with light wavelength, and it is possible to control which of the two spheres reaches a higher temperature. In particular, a temperature ratio in the 0.8−1.4 range is achievable for incidence along the dimer axis and wavelengths in the 550−650 nm range.

Linear Array of Gold Spheres. The contrast of temperature increase can be made higher in arrays formed by a larger number of particles. This is illustrated in Figure 6 for a chain of 15 gold spheres illuminated as shown in Figure 6a. The total absorption cross section of the array (Figure 6e) exhibits two maxima at 525 and 630 nm, which are directly translated into maxima of the partial absorption cross sections of the individual particles (Figure 6b,c). The shadowing effect noted for the dimer is also taking place in this chain, so that the upper spheres are more likely to absorb light that is directly impinging on them. This is the case for a wavelength of 525 nm, which corresponds to excitation of localized plasmons. However, the 630 nm feature is associated with propagating plasmons, and thus, the electromagnetic energy picked up by all spheres propagates down the chain and produces maximum absorption in its lower part, with softer replicas at intermediate positions originating in the standing waves set up by multiple reflections at the chain ends. This guided mode is strongly attenuated but sufficiently strong as to allow the maximum temperature change to be chosen at nearly arbitrary positions along the chain by just selecting the appropriate wavelength (Figure 6d). We hope that these preliminary results trigger further activity to explore the interplay between guided modes in particle chains[28,29] and the temperature distribution upon external illumination.

CONCLUSIONS

In conclusion, we have addressed the issue of quantitatively solving the temperature distribution in illuminated nanostructures, for which we have combined electromagnetic calculations and a solution of the heat diffusion equation under stationary conditions, formally equivalent the Poisson equation for the electrostatic problem. We have solved both Maxwell's equations for the electrodynamic calculation and Poisson's equation for the temperature distribution using a common boundary element method approach, with the distribution of electric field intensity predicted by the former acting as the source of the latter equation. The boundary element method provides rigorous solutions of these equations but requires only surface rather than volume parametrization, thus resulting in a significant reduction in computation time compared to other techniques (see refs 30 and 31). We have presented temperature distributions driven by plasmon excitation in gold single spheres, sphere dimers, and sphere chains immersed in water. We have also provided universal curves for a dimensionless thermal-capacitance coefficient that allows obtaining the temperature change of irradiated particles of various shapes (ellipsoids, rods, disks, and rings), using as input the absorption cross section, the light intensity, and the thermal conductivity of the surrounding medium.

Our methods have general applicability to nanostructures of arbitrary morphology by relying on full 3D implementations of the BEM.[30,31] A large degree of

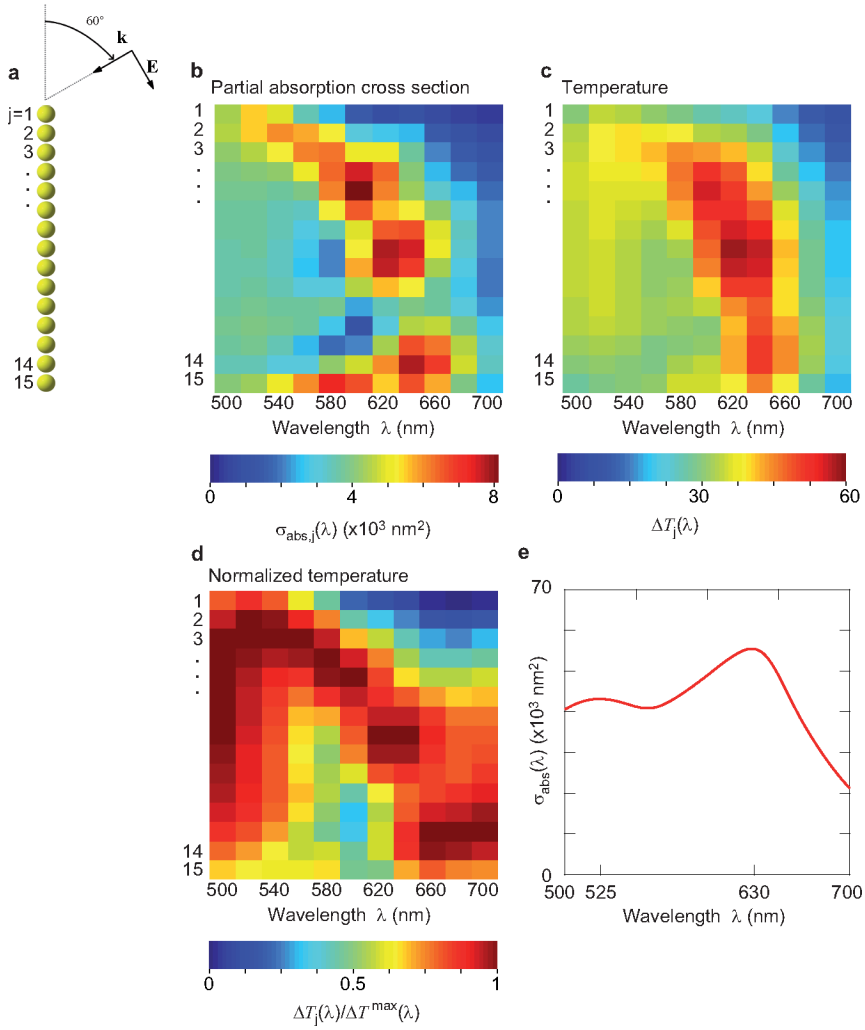

Figure 6. Photothermal heating in a nanoparticle array. (a) We consider a chain of 15 gold nanospheres surrounded by water and illuminated as shown in the drawing. The spheres are 50 nm in diameter, and the gap between consecutive particles is 5 nm. (b) Partial absorption cross section of each of the spheres as a function of light wavelength. (c) Temperature increase of the nanoparticles for 1 mW/μm² incident light intensity. (d) Temperature increase of the nanoparticles, normalized to the temperature increase of the hottest sphere for each wavelength. (e) Total absorption cross section of the array ($\sigma_{abs} = \sum_j \sigma_{abs,j}$).

control over the temperature increase of individual spheres has been shown to be attainable by playing with the illumination geometry and light wavelength. This can be viewed as a control over the distribution of photothermal nanosources, which are tuned to produce controllable temperature distributions on the nanoscale. Our work allows predicting accurate distributions of temperature driven in nanostructures by photothermal absorption. This opens a new route toward nanoscale control of local melting, thermal activation at the molecular level, and heat delivery in general, with potential applications to nanostructure shaping, drug delivery, and far-field steering of mechanical motion.

MATERIALS AND METHODS

Optical Simulations. The electric near-field and scattering cross sections for individual and arrayed spheres are calculated using the boundary element method, described elsewhere.[22,23] The calculations are contrasted to the multiple elastic scattering of multipole expansions (MESME) method,[26] and no differences are observed that can be discerned on the scale of the figures. Partial absorption cross sections are obtained in BEM for each particle by integrating the Poynting vector over a sphere surrounding it. These cross sections are also calculated in MESME from the coefficients of multipolar spherical waves in the vicinity of each particle. The material properties of gold are implemented into the calculations using the experimental dielectric function ε_{gold} measured by Johnson and Christy.[32] The water is considered to have a dielectric function $\varepsilon_{water} = 1.777$.

Thermal Diffusion Simulations. The Poisson equation, to which the thermal diffusion equation reduces in the steady-state regime, is solved to obtain Figure 2 using the BEM in the $\omega \to 0$ limit. For Figures 3−6, we have developed a new BEM implementation specialized for particles with uniform temperatures (UTA approximation). In particular, for an individual particle (*e.g.*, for the geometries considered in Figure 3), the temperature in the water can be expressed as

$$\Delta T(\mathbf{r}) = \int_S d\mathbf{s}' G(|\mathbf{r} - \mathbf{s}'|)\sigma(\mathbf{s}')$$

where $G(r) = 1/r$ is the Coulomb potential, the integral is extended over the particle surface, and σ is an auxiliary *thermal surface charge* distribution. For points **r** situated on the particle surface, using matrix notation, one obtains the linear equation $\Delta T_{NP} = G \cdot \sigma$, where ΔT_{NP} is the particle temperature increase. We solve this equation by discretizing the integral using direct matrix inversion to yield the surface charge $\sigma = G^{-1} \cdot \Delta T_{NP}$. Finally, the particle temperature and the surface charge are still undetermined up to an overall factor, which is determined from the absorption cross section and from the condition that the integrated surface charge yields the large-distance temperature of eq 5.

Acknowledgment. This work has been supported by the Spanish MICINN (MAT2007-66050 and Consolider NanoLight.es) and by the EU (NMP4-SL-2008-213669-ENSEMBLE). R.Q. thanks Fundació Cellex Barcelona.

REFERENCES AND NOTES

1. Ross, D.; Gaitan, M.; Locascio, L. E. Temperature Measurement in Microfluidic Systems Using a Temperature-Dependent Fluorescent Dye. *Anal. Chem.* **2001**, *73*, 4117–4123.
2. Liu, G. L.; Kim, J.; Lu, Y.; Lee, L. P. Optofluidic Control Using Photothermal Nanoparticles. *Nat. Mater.* **2005**, *5*, 27–32.
3. Pollock, H. M.; Hammiche, A. Micro-Thermal Analysis: Techniques and Applications. *J. Phys. D: Appl. Phys.* **2001**, *34*, R23U–R53.
4. Gobin, A. M.; Lee, M. H.; Halas, N. J.; James, W. D.; Drezek, R. A.; West, J. L. Near-Infrared Resonant Nanoshells for Combined Optical Imaging and Photothermal Cancer Therapy. *Nano Lett.* **2007**, *7*, 1929–1934.
5. Jain, P. K.; El-Sayed, I. H.; El-Sayed, M. A. Au Nanoparticles Target Cancer. *Nano Today* **2007**, *2*, 18–29.
6. Zhao, W.; Karp, J. M. Tumour Targeting: Nanoantennas Heat Up. *Nat. Mater.* **2009**, *8*, 453–454.
7. Skirtach, A. G.; Dejugnat, C.; Braun, D.; Susha, A. S.; Rogach, A. L.; Parak, W. J.; Möhwald, H.; Sukhorukov, G. B. the Role of Metal Nanoparticles in Remote Release of Encapsulated Materials. *Nano Lett.* **2005**, *5*, 1371–1377.
8. Pissuwan, D.; Valenzuela, S. M.; Cortie, M. B. Therapeutic Possibilities of Plasmonically Heated Gold Nanoparticles. *Trends Biotechnol.* **2006**, *24*, 62–67.
9. Barral, M. A.; Llois, A. M. Photothermal Imaging of Nanometer-Sized Metal Particles among Scatterers. *Science* **2002**, *297*, 1160–1163.
10. Berciaud, S.; Lasne, D.; Blab, G. A.; Cognet, L.; Lounis, B. Photothermal Heterodyne Imaging of Individual Metallic Nanoparticles: Theory *versus* Experiment. *Phys. Rev. B* **2006**, *73*, 045424.
11. Lasne, D.; Blab, G. A.; Berciaud, S.; Heine, M.; Groc, L.; Choquet, D.; Cognet, L.; Lounis, B. Single Nanoparticle Photothermal Tracking (SNaPT) of 5-nm Gold Beads in Live Cells. *Biophys. J.* **2006**, *91*, 4598–4604.
12. Baffou, G.; Kreuzer, M. P.; Kulzer, F.; Quidant, R. Temperature Mapping near Plasmonic Nanostructures Using Fluorescence Polarization Anisotropy. *Opt. Express* **2009**, *17*, 3291–3298.
13. Wang, L.; Li, B. Thermal Memory: A Storage of Phononic Information. *Phys. Rev. Lett.* **2008**, *101*, 267203.
14. Yang, N.; Zhang, G.; Li, B. Carbon Nanocone: A Promising Thermal Rectifier. *Appl. Phys. Lett.* **2008**, *93*, 243111.
15. Chang, C. W.; Okawa, D.; Majumdar, A.; Zettl, A. Solid-State Thermal Rectifier. *Science* **2006**, *314*, 1121–1124.
16. Cao, L.; Barsic, D. N.; Guichard, A. R.; Brongersma, M. L. Plasmon-Assisted Local Temperature Control to Pattern Individual Semiconductor Nanowires and Carbon Nanotubes. *Nano Lett.* **2007**, *7*, 3523–3527.
17. Govorov, A. O.; Richardson, H. H. Generating Heat with Metal Nanoparticles. *Nano Today* **2007**, *2*, 30–38.
18. Urban, A. S.; Fedoruk, M.; Horton, M. R.; Rädler, J. O.; Stefani, F. D.; Feldmann, J. Controlled Nanometric Phase Transitions of Phospholipid Membranes by Plasmonic Heating of Single Gold Nanoparticles. *Nano Lett.* **2009**, *9*, 2903–2908.
19. Baffou, G.; Quidant, R.; Girard, C. Heat Generation in Plasmonic Nanostructures: Influence of Morphology. *Appl. Phys. Lett.* **2009**, *94*, 153109.
20. Pileni, M. P. Control of the Size and Shape of Inorganic Nanocrystals at Various Scales from Nano to Macrodomains. *J. Phys. Chem. C* **2007**, *111*, 9019–9038.
21. Stokes, N.; McDonagh, A. M.; Cortie, M. B. Preparation of Nanoscale Gold Structures by Nanolithography. *Gold Bull.* **2007**, *40/4*, 310–320.
22. García de Abajo, F. J.; Howie, A. Relativistic Electron Energy Loss and Electron-Induced Photon Emission in Inhomogeneous Dielectrics. *Phys. Rev. Lett.* **1998**, *80*, 5180–5183.
23. García de Abajo, F. J.; Howie, A. Retarded Field Calculation of Electron Energy Loss in Inhomogeneous Dielectrics. *Phys. Rev. B* **2002**, *65*, 115418.
24. Richardson, H. H.; Carlson, M. T.; Tandler, P. J.; Hernandez, P.; Govorov, A. O. Experimental and Theoretical Studies of Light-to-Heat Conversion and Collective Heating Effects in Metal Nanoparticle Solutions. *Nano Lett.* **2009**, *9*, 1139–1146.
25. Eckert, E. R. G.; Drake, R. M. *Heat and Mass Transfer*; McGraw-Hill: New York, 1959.
26. García de Abajo, F. J. Multiple Scattering of Radiation in Clusters of Dielectrics. *Phys. Rev. B* **1999**, *60*, 6086–6102.
27. Romero, I.; Aizpurua, J.; Bryant, G. W.; García de Abajo, F. J. Plasmons in Nearly Touching Metallic Nanoparticles: Singular Response in the Limit of Touching Dimers. *Opt. Express* **2006**, *14*, 9988–9999.
28. Quinten, M.; Leitner, A.; Krenn, J. R.; Aussenegg, F. R. Electromagnetic Energy Transport *via* Linear Chains of Silver Nanoparticles. *Opt. Lett.* **1998**, *23*, 1331–1333.
29. Maier, S. A.; Kik, P. G.; Atwater, H. A.; Meltzer, S.; Harel, E.; Koel, B. E.; Requicha, A. A. G. Local Detection of Electromagnetic Energy Transport below the Diffraction Limit in Metal Nanoparticle Plasmon Waveguides. *Nat. Mater.* **2003**, *2*, 229–232.
30. Myroshnychenko, V.; Carbó-Argibay, E.; Pastoriza-Santos, I.; Pérez-Juste, J.; Liz-Marzán, L. M.; García de Abajo, F. J. Modelling the Optical Response of Highly Faceted Metal Nanoparticles with a Fully 3D Boundary Element Method. *Adv. Mater.* **2008**, *20*, 4288–4293.
31. Myroshnychenko, V.; Rodríguez-Fernández, J.; Pastoriza-Santos, I.; Funston, A. M.; Novo, C.; Mulvaney, P.; Liz-Marzán, L. M.; García de Abajo, F. J. Modelling the Optical Response of Gold Nanoparticles. *Chem. Soc. Rev.* **2008**, *37*, 1792–1805.
32. Johnson, P. B.; Christy, R. W. Optical Constants of the Noble Metals. *Phys. Rev. B* **1972**, *6*, 4370–4379.